Available online at www.sciencedirect.com

jmr&t
Journal of Materials Research and Technology

journal homepage: www.elsevier.com/locate/jmrt

Mixed mode brittle fracture of stereolithographic 3D-printed parts

Mohammad Reza Khosravani [a,*], *Peter Frohn-Sörensen* [b], *Bernd Engel* [b], *Tamara Reinicke* [a]

[a] Chair of Product Development, University of Siegen, Paul-Bonatz-Str. 9-11, 57068 Siegen, Germany
[b] Chair of Production Technologies, University of Siegen, Breite Strasse 11, 57076 Siegen, Germany

ARTICLE INFO

Article history:
Received 2 March 2023
Accepted 16 June 2023
Available online 21 June 2023

Keywords:
Additive manufacturing
Mixed mode I/II
Fracture
SLA
DIC

ABSTRACT

Technical advances in additive manufacturing (AM), also known as three-dimensional (3D) printing, have led to applications of this technology in creation of end-use items. Consequently, performance and the mechanical strength of AMed parts have become of significant importance. In this research, fracture behavior and crack propagation of AMed cracked plates are investigated. To this aim, the stereolithography (SLA) technique is used to fabricate square plate specimens with a hole in the center and radial cracks that started at the perimeter of the central hole. Here, full range of mixed-mode fracture (from pure mode I to pure mode II) are obtained by altering the angle between the crack and the applied load. We used the finite element method to determine stress intensity factors. This study deals with a series of experiments on 3D-printed cracked plates to study mixed-mode fracture and crack propagation in brittle fracture of SLA 3D-printed components. Additionally, the digital image correlation technique was used to determine strain field on the surface of the specimens. As SLA is one of the most commonly used concepts in polymer 3D printing and has garnered significant attention for fabrication of complex structural elements, the outcomes of this study are useful for next developments and innovative designs of 3D-printed polymeric components.

1. Introduction

Conventional manufacturing techniques such as milling and grinding have limitations in terms of complexity, product size, and material loss. In contrast, additive manufacturing (AM) offers high versatility that can be utilized for fabrication of geometrically complex components. AM also known as three-dimensional (3D) printing, is an innovative manufacturing technique for production of components through layer by layer deposition mechanism [1]. Since 3D printing is a tool-free technique, it reduces wear and machine setup times. Moreover, 3D printing is flexible in product design and it overcomes the design limitations associated with subtractive manufacturing techniques. Due to these advantages, different AM processes have been used for fabrication of structural elements in divers applications, such as food industry [2], medicine [3], aerospace [4], healthcare monitoring [5], tooling and molding industries [6], robotics [7], and construction [8]. The American Society for Testing and Materials (ASTM) [9], has classified 3D printing into different techniques of which Vat photopolymerization (VP) is used in the present study.

* Corresponding author.
E-mail address: mohammadreza.khosravani@uni-siegen.de (M.R. Khosravani).
https://doi.org/10.1016/j.jmrt.2023.06.175

VP is a type of 3D printing process which utilizes a light source to cure photopolymer resin in a vat. There are two types of VP technologies that are most frequently used: (i) stereolithography (SLA) printing, where the hardening of liquid resin occurs by a high-powered laser, and (ii) digital light processing (DLP), where polymerization of the layer is based on LED projectors. Photopolymers are thermosets that are activated upon exposure to radiation, typically in the ultraviolet light or visible light spectrum, and they are widely used as raw material for VP process [10]. Currently, there are two possible structures for a VP printer depending on the manufacturer design: bottom-up and top-down orientations [11]. SLA has been widely utilized in various fields, because of its benefits in fabrication of structural elements with complicated geometry at high precision and repeatability in reduced time compared to traditional manufacturing.

Despite early applications of 3D printing for creating prototypes, it is being utilized for manufacturing of final products. Consequently, the structural integrity and the mechanical strength of AMed parts have become of great importance. In this context, several research studies have been performed to investigate mechanical behavior and strength of different AMed parts [12–17]. For instance, in [18] dynamic behavior of 3D-printed composite was studied. In this respect, the specimens were fabricated using material extrusion process. Based on the test via Hopkinosn bar, dynamic compression behavior of 3D-printed part was determined. Later, in [19] polylactic acid (PLA) and recycled PLA were utilized to print the specimens. Tensile, impact, and bending strength of 3D-printed parts were determined according to the applicable test standards. According to the obtained results it was concluded that PLA had stronger tensile strength than recycled PLA at all layer thicknesses. However, literature investigations and previous experimental tests [20–23] confirmed that the physical appearance and mechanical properties of AMed parts are mainly characterized by printing parameters and utilized materials.

The impact of printing orientation on the tensile strength of SLA 3D-printed parts was studied in [24]. To this aim, the dumbbell-shaped specimens were fabricated in different orientations and tensile tests were conducted. The documented results showed that there are relatively small differences regarding ultimate tensile stress or modulus of elasticity in the examined specimens. This result is similar with a previous study, where Hague et al. [25] reported that biggest changes in mechanical characteristics of SLA 3D-printed parts are less than 5%. Therefore, it was concluded that the SLA technique produces broadly isotropic components and the printing direction has a little influence on the mechanical properties of components. An extant study [26] examined SLA 3D-printed components and confirmed that printing orientation has no effect on the mechanical properties of the SLA 3D-printed structural elements.

In the first virtual European Conference on Fracture, Li et al. [27] proposed a holed-cracked square plate (HCSP) specimen to study mixed mode I/II fracture in brittle materials. Although there are several research works on the fracture behavior of AMed components made by material extrusion process, to the best of the authors knowledge there is no study on the mixed mode I/II fracture of SLA 3D-printed components. Therefore, here we used the HCSP specimen configuration, which is suitable to obtain a full range of fracture mode mixities from pure mode I to pure mode II.

The aim of the current study is to examine mixed-mode fracture in SLA 3D-printed parts. To this end, HSCP specimens are printed with different crack orientation angles. According to the fracture tests under static loading conditions and finite element model (FEM), the fracture behavior and stress intensity factors are determined. In addition, we used the digital image correlation (DIC) technique to determine local deformation on the specimens surface, strain distribution at crack tip, and local displacements of tools. The presented results can be used for design and simulation of structural elements. In the reminder of the paper we proceed as follows: the next section presents the numerical analysis of hole-cracked specimens. In section 3, the details of specimen preparation and experimental tests are explained. Discussion on the obtained results and verification of experiments using the DIC technique have been presented in 4. Finally, we conclude the main findings of this research in Section 5.

2. Numerical analysis of hole-cracked specimens

The test of the HCSP specimens with respect to crack orientation angle is implemented into a simulation model utilizing the FEM. Considering the principal kinematics of the experiment (i.e., a linear displacement of both pins in opposite vertical direction), an elastic deformation analysis is calculated in an explicit simulation. The model is established and numerically solved in the software ABAQUS CAE 2021 by Dassault Systémes. Both pins are represented by rigid shells, as their steel material is nearly a hundred times stiffer than the polymer material of the HCSP specimens. The HCSP is discretized by deformable C3D8R linear brick elements, with an adaptive meshing from a fine 0.25 mm mesh at the inner hole and crack surfaces towards a coarser 4 mm mesh at the outer square shape of the HCS plate. In particular, the inner cracks are modeled with the width as resulting from 3D printing plus additional narrow outer slits, which are applied to the physical specimens by a sawing machine. The nominal thickness of the saw blade (i.e., 0.25 mm), was given as width for the sharp crack in the model. Each model in the simulations included a total of about 410,000 elements. In the simulation, the variation of crack orientation angle was modeled according to the practical experiments. The utilized resin material is implemented in the simulations by means of its mechanical elastic properties obtained from the tensile tests of the present study. Moreover, density is taken from the material supplier's data sheet [28].

In the current simulations, the contact interactions between pins and HCSP are modeled as hard contacts in the element normal direction, while tangential behavior was modeled by a constant Coulomb's law. The edges of the HCSP are constrained from any out–of plane movements like in the fixture of the experiments. With all other degrees of freedom locked, a constant vertical velocity is applied to the pins in opposite vertical direction to simulate the loading conditions

of the experimental tests. The simulation runs until a relative displacement of 0.8 mm is achieved in between both pins, which agrees with the maximum displacement achieved in the experiments with respect to local displacement as obtained from DIC, thus excluding clearances and machine stiffness. The numerical simulations are solved on five parallelized processors with double explicit analysis precision and full nodal output precision.

From these simulations, the stress maps at maximum deformation are evaluated. The FEM is used to determine the dimensionless parameters of Y_i and T^* for the test coupon under different fracture modes. The stress gradients at the HCSP surfaces are all presented in Fig. 1 with respect to the crack angles. All stress distributions are scaled equally from zero to 38 MPa. In fact, the distinct von Mises equivalent stress distributions are scaled for comparison. Here, the crack angles

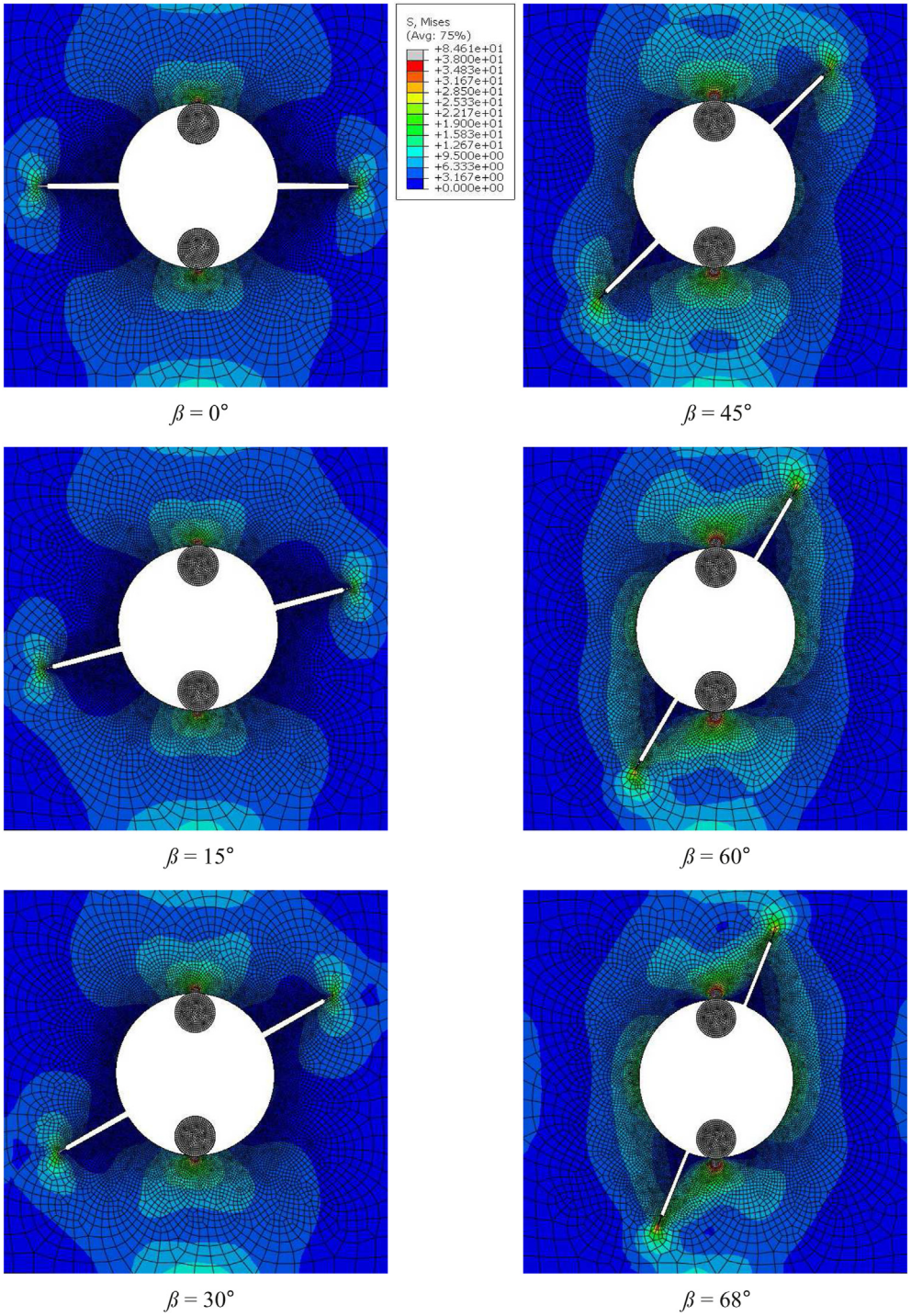

Fig. 1 – Numerical fracture load studies at HCSP. Variation of the crack orientation angle and corresponding von Mises stress distributions obtained from FE simulations.

are varied successively in steps of 15° beginning from 0° (pure mode I fracture) up to 60° with an additional angle of 68°, which was identified to correspond to pure mode II fracture [27].

The illustrated maximum stress value is scaled corresponding to the material's ultimate tensile strength obtained from uniaxial tensile tests. In the contact area between pins and HCSP, pronounced local compressive stresses are observed in simulation and the experimental practices. At the crack tips of the horizontal, 0° crack orientation, a butterfly-shaped stress distribution is observed which is found in a symmetrical pattern and reaches out towards approximately ±45°. With beginning crack inclination, this distribution shape transforms through the mixed modes until reaching a single, co-linear club-shaped distribution reaching out from the crack tip of 68° HCSP, which represents pure mode II. Indeed, by an increase in β, the von Mises stress contours appear asymmetric regarding to the crack plane. In Fig. 2, an example for a such distribution is shown for the mixed mode I/II obtained at 45° crack orientation angle.

The adaptive FE mesh discretization strategy leads to even brick-shaped FEM, which are capable of calculating the stress distribution in sufficient detail for further studies.

3. Experimental procedure

3.1. Specimen fabrication

In the current study, we used a Formlabs 3D printer (Form 2) to fabricate the test samples. The build volume of the utilized 3D printer is approximately 145 × 145 × 175 mm (XYZ). Here, we used Phrozen TR300 resin and the printing parameters which are recommended by the resin suppliers were considered for fabrication of the specimens [28]. In this research, two groups of test samples were prepared: (i) dumbbell-shaped test coupons, and (ii) HCSP specimens.

Here, the dumbbell-shaped specimens were designed in accordance with Type I ASTM D638 [29] to obtain basic mechanical properties based on the tensile test. A computer aided design (CAD) platform was utilized to design all specimens, and the files were sequentially saved in ".stl" format. These files were utilized for fabrication based on the SLA process. After the printing process, it was necessary to conduct a post-print curing. In this study, the dumbbell-shaped specimens were cured by ultraviolet LED light in different positions and 10 min for each direction to make sure that there is no uncured resin in 3D-printed parts. It is noteworthy that 3D-printed dumbbell-shaped samples become more stable and rigid as a result of this post-print curing. We printed and examined four dumbbell-shaped specimens.

Similar to the dumbbell-shaped test coupons, we used a CAD platform and the SLA process for design and fabrication of HCSP specimens. These specimens are square plates with a thickness of B and an edge length of W. There is a hole in the center with diameter D and radial cracks started at perimeter of the central hole. Here, $2a$ is the distance between two crack tips. Fig. 3 shows a schematic of an HCSP specimen ($W = 80$ mm, $B = 10$ mm, $D = 32$ mm, and $2a = 64$ mm). Cracks in the specimens are printed based on the CAD file and after the printing process we used a sawing machine to introduce a more sharpened crack. After fabrication of HCSP specimens, cracks were visually checked to ensure the correct shape of the crack tip.

Altering the crack direction relative to the loading orientation (specified by the inclination angle β) provides different cases of mixed mode I/II. Particularly, the crack flanks open without sliding, when the crack is orientated in the direction of the applied load. Therefore, there is pure mode I loading. Here, we have printed specimens with different β equal to 0°, 15°, 30°, 45°, 60°, and 68° to see fracture mode mixities including pure mode I, pure mode II, and mixed mode I/II. By this configuration, the mixed mode loading condition can be easily reached, which is an advantage, and compared to other center cracked samples, the hole is more convenient to introduce the crack [30–32]. 3D-printed specimens with different β are illustrated in Fig. 4. Since SLA-printed parts are isotropic, printing direction has no influence on the mechanical characterization of the fabricated specimens.

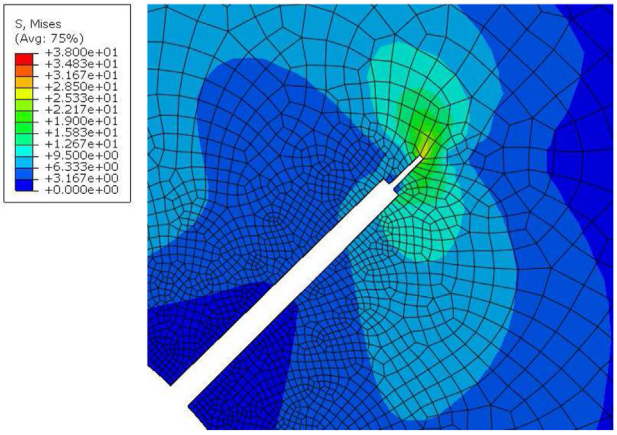

Fig. 2 – FE results of the von Mises stress distribution in a 45° specimen.

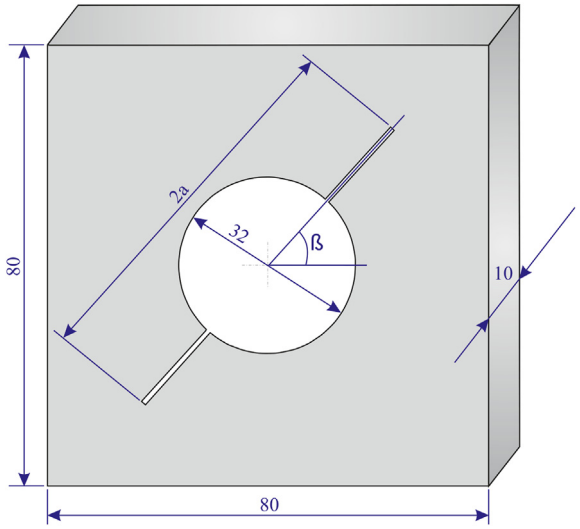

Fig. 3 – A schematic of HCSP specimens (dimensions in mm).

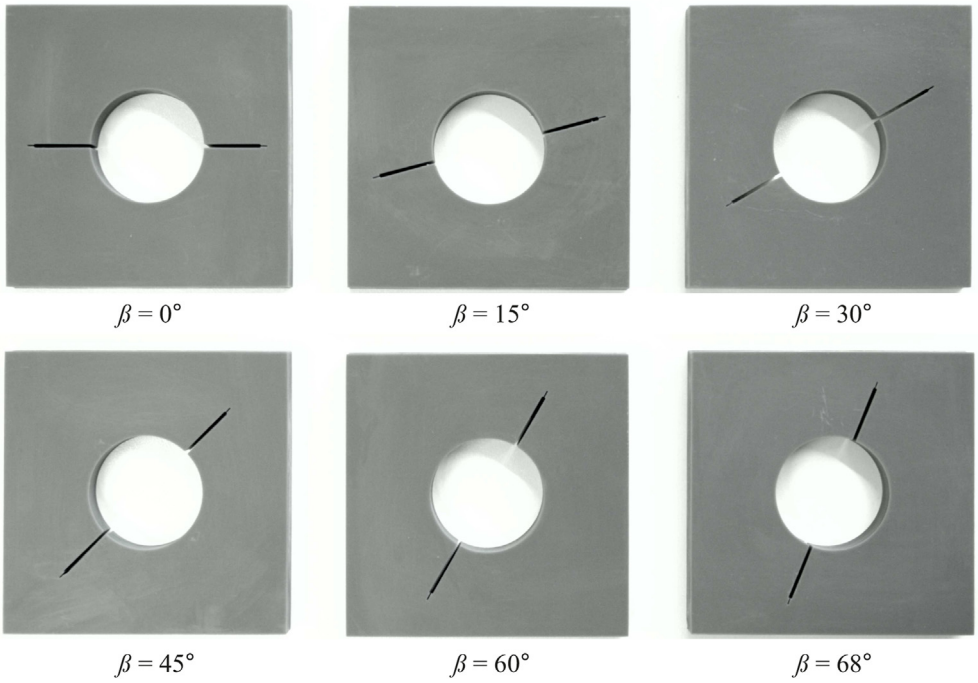

Fig. 4 – 3D-printed HCSP specimens with different crack angles.

It is noteworthy that all 3D-printed specimens were stored in a dark environment to avoid additional curing and in a controlled environment (50% relative humidity & 20 °C) prior to the tests. In this study, for each crack angle, seven identical HCSP specimens were examined to ensure repeatability and reproducibility of the results. All test coupons were subjected to the tensile test that would be explained in the next subsections.

3.2. *Tensile tests of 3D-printed dumbbell-shaped samples*

A series of tensile tests was conducted on the dumbbell-shaped test coupons. To this aim, we used a Zwick/Roell Z250 machine, which has a cross-head speed up to 10 mm/s. The testing machine was equipped with a 250 kN load cell of the accuracy class 0.02%. The wedge grips of the machine clamps the shoulder area of the test coupons firmly. According to ASTM D638 [29], uniaxial tensile load was applied to the samples. The utilized grips held the test coupons perfectly aligned in the vertical direction. In this study, a constant crosshead speed of 5 mm/min was applied until failure of the specimens. Also, prior to the test start, we applied a preload of 5 N to the specimen to eliminate grippers' slack. Geometries of a dumbbell-shaped specimen and its tensile test conditions are schematically illustrated in Fig. 5.

3.3. *Experimental practices on HCSP specimens*

In the experimental practices, all HCSP specimens were subjected to tensile load in Zwick/Roell Z250 machine, which was already used for dumbbell-shaped test coupons. To this end, an appropriate fixture was designed and fabricated using 1.0503 tool steel. The main purpose of the fixture is to apply tensile load in between both pins which reach through the central hole of the HCSP specimen. Moreover, the fixture guides the front and backside of the specimen form any lateral displacement and avoids any specimen rotation around its central hole. All fracture tests were conducted under the displacement-control condition at rate of 2 mm/min. A series

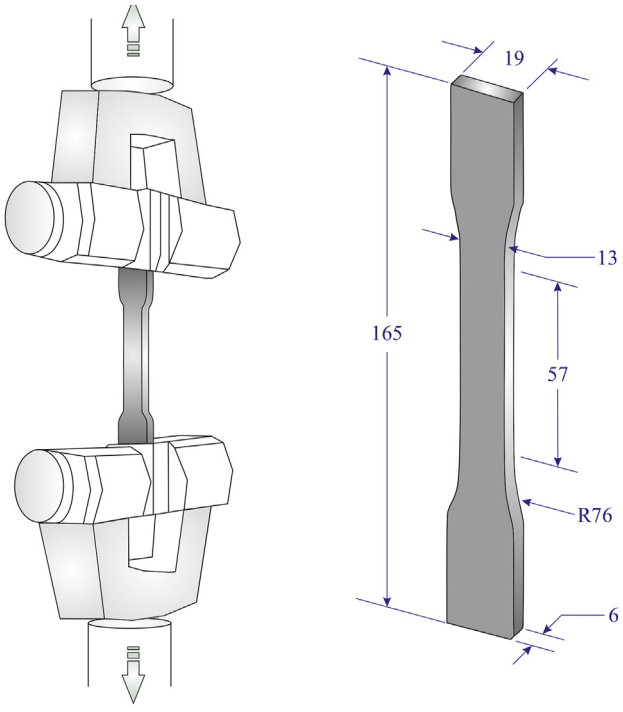

Fig. 5 – Geometries of a dumbbell-shaped specimen and schematic of tensile test conditions (dimensions in mm).

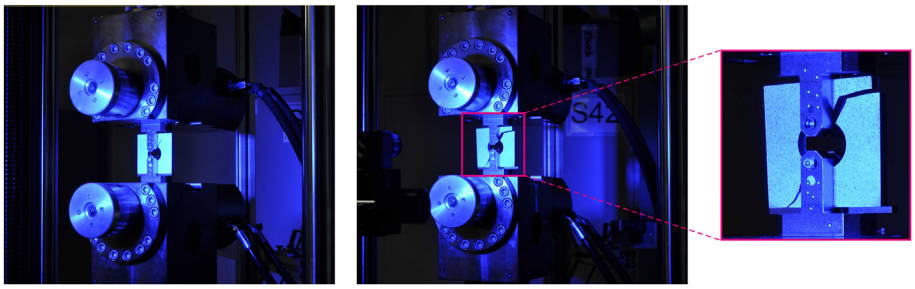

Fig. 6 – A 3D-printed HCSP specimen before and after applying load.

of tensile tests on HCSP specimens was carried out at room temperature (RT) conditions. Fig. 6 shows a HCSP specimen under tensile test conditions prior and after loading.

In the fracture tests on HCSP samples, the load–displacement curve was recorded at RT for each specimen and the load corresponding to fracture initiation (i.e., the maximum load) is considered as critical load. In fact, once the load reached to this critical level, all test samples suddenly fractured at the crack tips. After fracture, the HCSP specimens were released from the fixture for further crack evaluation.

4. Results and discussion

4.1. *Results of tensile tests on dumbbell-shaped specimens*

Based on the tests of the dumbbell-shaped samples, material properties such as tensile modulus and yield strength were determined. The obtained mechanical properties of the examined test coupons are summarized in Table 1. Those properties were also applied in the FEM simulations. In Table 1, E denotes Young's modulus at the elastic area of the stress–strain relationship, and S denotes ultimate tensile strength. Moreover, ϵ_f indicates the value of strain at fracture, and S_y denotes yield strength. Representative load–displacement curves and the stress–strain relationship obtained from tensile tests on the dumbbell-shaped samples are illustrated in Fig. 7.

Evidently a brittle deformation behavior of the utilized material is observed from the curves. The elastic tensile modulus E was evaluated from the secant in the interval between 5 and 15 MPa where the best linear compliance of the test repetitions was found in the stress–strain relation. The presented mechanical material parameters confirm the manufacturer's datasheet in general with an even higher tensile strength obtained in the present study.

Table 1 – Tensile properties of examined dumbbell-shaped specimens.

Tensile modulus E (MPa)	Ult. tensile strength S (MPa)	Fracture strain ϵ_f (%)	Yield strength S_y (MPa)
1888 ± 98	38.8 ± 3.1	3.0 ± 0.3	29.5 ± 1.1

4.2. *Results of experiments on HCSP specimens*

During the fracture tests, the load–displacement curves of the specimens with various orientation angles were documented up to the final fracture. Typical load–displacement curves of HCSP test coupons are illustrated in Fig. 8. After achieving a critical load, all specimens fractured instantly at the crack tips. It should be pointed out that the tests on HCSP test coupons confirmed that the fracture load increased with an increase in the crack orientation angle which is demonstrated in Fig. 8.

The HCSP specimens experienced pure mode I when $\beta = 0$. In the HCSP specimens, mixed-mode and pure mode II can be achieved by varying crack angle. As discussed in [27], in HCSP specimen, mode I and mode II stress intensity factors (K_I and K_{II}) and the non-singular term namely T-stress are functions of the geometry and depend on the orientation angle β, ratio of crack length to edge length $2a/W$, and diameter to the square plate length ratio D/W. This can be expressed as follows:

$$K_i = \frac{P}{B(W-D)}\sqrt{\pi a Y_i} \qquad i = I, II \tag{1}$$

$$T = \frac{P}{B(W-D)}T^* \tag{2}$$

where Y_I and Y_{II} are the geometry factors related to mode I and mode II, respectively. Also, T-stress is expressed as T^* in a normalized form. In [27], FE was used to calculate the geometry factors and T^* for different crack orientation angles (β) in HCSP specimens. Fig. 9 left, shows the values of Y_I, Y_{II}, and T^* for different crack orientation angles (β). In HCSP specimens, when $D/W = 0.4$ and $2a/W = 0.8$, there is pure mode I conditions ($\beta = 0^\circ$) and $Y_{II} = 0$. By increasing in the crack orientation angle (β) from 0° to 68°, the mode II geometry factor (Y_{II}) increases while mode I geometry factor (Y_I) decreases. In pure mode II, the crack orientation angle (β) is equal to 68° considering $D/W = 0.4$ and $2a/W = 0.8$ in HCSP specimens. For better understanding of the contributions of mode I and mode II stress intensity factors of each β, the relationship between β and mode mixity is illustrated in Fig. 9 right. In this respect, parameter M_e is specified as follows to show mode mixity:

$$M_e = \frac{2}{\pi}\arctan\left(\frac{K_I}{K_{II}}\right) \tag{3}$$

It is noteworthy that M_e has a value ranging from 0 to 1. Indeed, $M_e = 1$ represents pure mode I fracture, while $M_e = 0$ denotes pure mode II. By changing the crack orientation angle

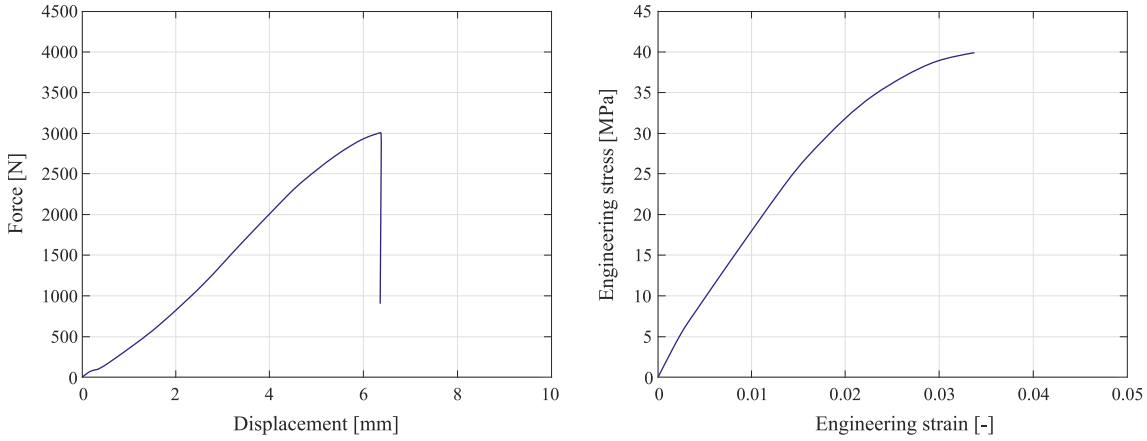

Fig. 7 – The load–displacement and stress–strain relationship of the dumbbell-shaped specimens.

in HCSP specimens, the state of mode mixity would be changed.

In HCSP test coupons, by varying the crack orientation angle, the condition of mode mixity and the proportion of sliding and opening deformation modes changed smoothly. This phenomenon in HCSP specimens is comparable to short bend beam samples, as presented in [33]. As it shown in [27], the HCSP test coupons obtained pure mode II fractures at inclination angles ranging from 58° to 68°, indicating that the HCSP sample is faced with a considerable orientation angle which leads to crack deformation change and shift from pure mode I fracture to pure mode II. In contrast, in short bend beam specimens the orientation angles for pure mode II are typically between 20° and 30°. In comparison, mode mixity in HCSP test coupons is generally unaffected by small variations in the crack orientation angle.

4.3. *Generalized strain energy density for HCSP specimens*

In this subsection, we present the application of the generalized strain energy density (GSED) in the fracture of 3D-printed HCSP specimens. Although the minimum strain energy density (SED) criterion has been used in several research studies, in an extant study [34], the SED criterion has been modified by considering T-stress entitled GSED for the analysis of fracture in quasi-brittle and brittle materials. In [35], based on the proposed airy stress function, the elastic stress field near to the crack tip was determined as infinite series expansions:

$$\sigma_{rr} = \frac{1}{\sqrt{2\pi r}}\cos\frac{\theta}{2}\left[K_I\left(1+\mathrm{Sin}^2\frac{\theta}{2}\right)+K_{II}\left(\frac{3}{2}\cos\theta-2\tan\frac{\theta}{2}\right)\right] + T\cos^2\theta+O\left(r^{\frac{1}{2}}\right) \quad (4)$$

$$\sigma_{\theta\theta} = \frac{1}{\sqrt{2\pi r}}\cos\frac{\theta}{2}\left[K_I\cos^2\frac{\theta}{2}-\frac{3}{2}K_{II}\sin\theta\right]+T\sin^2\theta+O\left(r^{\frac{1}{2}}\right) \quad (5)$$

$$\sigma_{r\theta} = \frac{1}{2\sqrt{2\pi r}}\cos\frac{\theta}{2}\left[K_I\,\mathrm{Sin}\,\theta+K_{II}(3\cos\theta-1)\right]-T\sin\theta\cos\theta + O\left(r^{\frac{1}{2}}\right) \quad (6)$$

where σ_{rr}, $\sigma_{\theta\theta}$, and $\sigma_{r\theta}$ denote elastic stress components in polar coordinate system. Also, r and θ indicate conventional tip of crack coordinates. Moreover, K_I and K_{II} indicate stress intensity factors in modes I and II, respectively, depending on the geometry of specimens and loading conditions. T is the T-stress, and the higher order terms $O(r^{\frac{1}{2}})$ is negligible around crack tip.

The GSED criterion considers the effect of the T-stress term and critical distance (r_c), as well as singular terms obtained

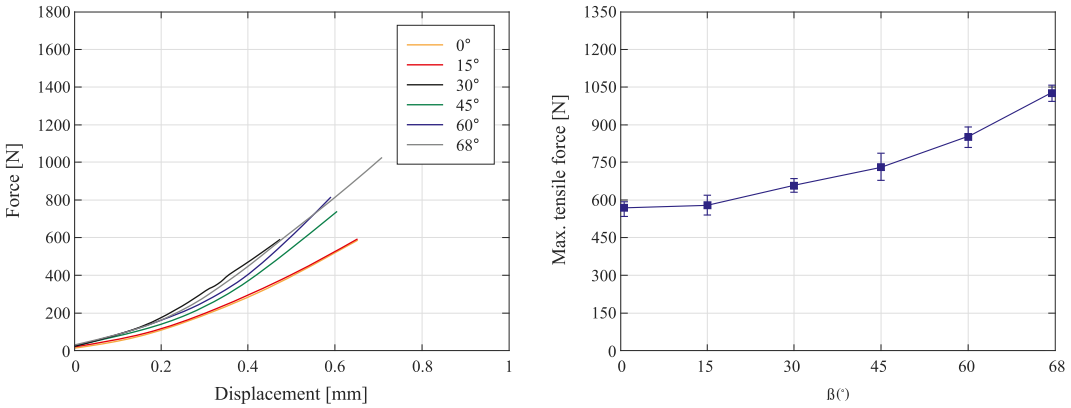

Fig. 8 – The load–displacement curves (left) and max. tensile force vs crack angle (right) of 3D-printed HCSP specimens.

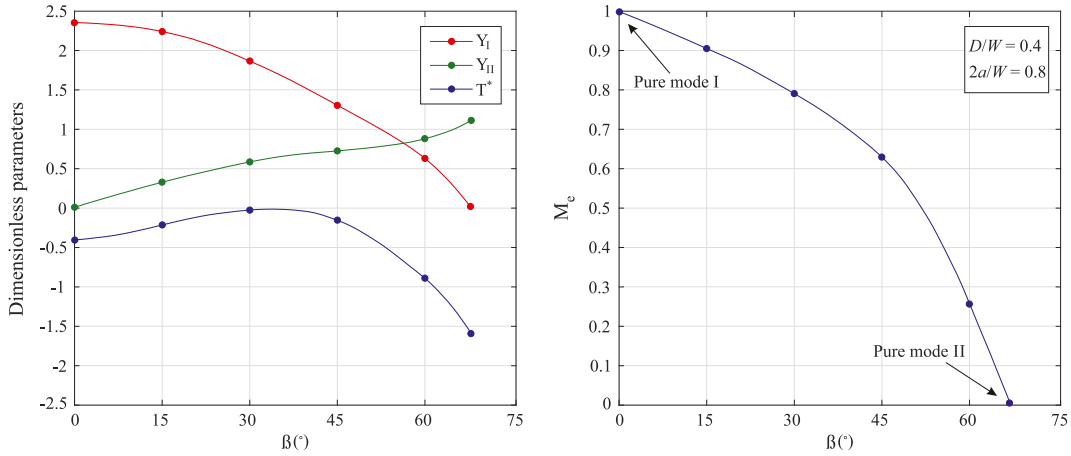

Fig. 9 – Dimensionless parameters (Y_I, Y_{II}, and T*) versus orientation angle (left), and the relationship between orientation angle (β) and mode mixity (right).

from the Williams series expansion near to the crack tip. For plane problems, the strain energy density function (dw/dv) stored in an element is defined as follows:

$$\frac{dW}{dV}=\frac{1}{2G}\left[\frac{K+1}{8}(\sigma_{rr}+\sigma_{\theta\theta})^2-\sigma_{rr}\sigma_{\theta\theta}+\sigma_{r\theta}^2\right] \tag{7}$$

where $G = E/2(1+\nu)$ is the shear modulus of elasticity, and K is an elastic constant and equal to (3-ν)/1+ν and 3-4ν for plane stress and plane strain problems, respectively. S is the strain energy density factor and represents the strength of the elastic energy field in the vicinity of the crack tip:

$$S=r\frac{dW}{dV}=\frac{r}{2G}\left[\frac{K+1}{8}(\sigma_{rr}+\sigma_{\theta\theta})^2-\sigma_{rr}\sigma_{\theta\theta}+\sigma_{r\theta}^2\right] \tag{8}$$

S can be calculated by substituting elastic stress components in polar coordinates into Eq. (7), and simplifying Eq. (8);

$$S=\frac{1}{16\pi G}\left[a_1K_I^2+a_2K_{II}^2+2a_3K_IK_{II}+a_4\left(\sqrt{2\pi r}\right)K_I\,T+a_5\left(\sqrt{2\pi r}\right)K_{II}T+a_6(2\pi r)T^2\right] \tag{9}$$

where the coefficients $a_i(i=1-6)$ are given by:

$$a_1=(K-\cos\theta)(1+\cos\theta) \tag{10}$$

$$a_2=[K(1-\cos\theta)+\cos\theta(1+3\cos\theta)] \tag{11}$$

$$a_3=\mathrm{Sin}\,\theta(2\,\mathrm{Cos}\,\theta-(K-1)) \tag{12}$$

$$a_4=\mathrm{Cos}\,\frac{\theta}{2}(\mathrm{Cos}\,(2\theta)-\mathrm{Cos}\,\theta+(k-1)) \tag{13}$$

$$a_5=-\mathrm{Sin}\,\frac{\theta}{2}(\mathrm{Cos}\,(2\theta)+\mathrm{Cos}\,\theta+(k+1)) \tag{14}$$

$$a_6=\frac{(K+1)}{2} \tag{15}$$

Based on the GSED criterion, the crack growth occurs along the direction $\theta_\circ$ where at a critical distance from tip of the crack r_c, S is the minimum. The crack propagation angle and and fracture toughness for mixed mode I/II can be calculated utilizing the following equations:

$$\frac{\partial s}{\partial\theta}|_{\theta=\theta_0}\rightarrow[K_I\sin\,\theta_\circ+K_{II}(3\cos\theta_\circ-1)]-\frac{16T}{3}\sqrt{2\pi r_c}\cos\theta_\circ\sin\frac{\theta_\circ}{2}=0 \tag{16}$$

$$K_{Ic}=\cos\frac{\theta_\circ}{2}\left[K_I\cos^2\frac{\theta_\circ}{2}-\frac{3}{2}K_{II}\sin\,\theta_\circ\right]+\sqrt{2\pi r_c}\,T\sin^2\theta_\circ \tag{17}$$

In [36], it has been discussed how these equations were derived, where Smith et al. have explained that sign and magnitude of T have considerable effect on the mixed mode brittle fracture. In fact, in contrast to positive T, a negative T increases fracture toughness in the mixed mode fracture.

Based on the GSED criterion, dimensionless parameters K_I, K_{II}, T*, and the critical distance (r_c), should be known for prediction of fracture toughness in mixed mode fracture. r_c can be considered as size of the fracture process zone which is independent of the loading conditions and the geometry of the specimen. Schmidt [37], proposed a theoretical model to estimate the size of the critical distance:

$$r_c=\frac{1}{2\pi}\left(\frac{K_{Ic}}{\sigma_t}\right)^2 \tag{18}$$

where K_{Ic} is the fracture toughness in mode I, and σ_t the material tensile strength. Eq. (9), Eq. (16), and Eq. (17) are used and also Y_I, Y_{II}, T* are extracted from Fig. 7 to determine fracture toughness from pure mode I to pure mode II in HCSP test coupons. The obtained results are summarized in Table 2. These findings are in agreement with reported results in [38], where Brugo et al. investigated mixed-mode I and II fracture of semicircular polyamide specimens with radial edge-crack. Since mode II has a wider stress state distribution, higher fracture toughness values are recorded for this mode.

The Fracture tests indicate that in all specimens fracture started at the initial crack tip. The fractured specimens with different crack orientation angles are illustrated in Fig. 10. Only under pure mode I conditions, the crack propagates in

Table 2 – The results of fracture tests on HCSP specimens.

Crack orientation (β)	Crack propagation angle (θ_o)	Fracture load P_{cr}(N)	Stress intensity factor K_I (MPa$\sqrt{m}$)	Stress intensity factor K_{II} (MPa$\sqrt{m}$)
0°	0°	568.1	0.781	0
15°	−14.7°	598.5	0.693	0.194
30°	−29.2°	655.2	0.574	0.389
45°	−44.6°	708.8	0.482	0.521
60°	−55.1°	778.2	0.328	0.645
68°	−61.5°	1066.2	0	0.823

the same direction as the original crack. In mixed-mode I/II fracture, the crack growth path is distinct from the direction of the initial crack.

In the present study, we used a free-angle observation system (VHX-S90F) for visual inspection of the fractured specimens. In this context, we examined the fracture surface of all SLA 3D-printed specimens under different mode mixities to determine the crack propagation angle (θ_o) in different specimens. In detail, a photo of each fractured specimen was taken by the above-mentioned observation system and a tangent line was drawn from the crack tip along the crack propagation direction. The crack propagation angle was achieved by measuring the angle between the original crack line and the tangent line of the crack growth direction. Measured crack propagation angles are summarized in Table 2 for different specimens. In addition, the GSED criterion can be used to determine θ_o. Fig. 11 shows the crack propagation angle in a fractured specimen. Also, the comparison of experimental observation and prediction of crack propagation angle by GSED is depicted in Fig. 11. Evidently, there is a good agreement between test results and theoretical predilection by the GSED criterion.

The conducted experiments confirmed brittle fracture in SLA 3D-printed parts. It was observed that in the mixed-mode fracture of 3D-printed parts, the crack propagates along curvilinear paths rather than following the initial crack line.

4.4. *Verification of fracture tests by DIC*

The method of DIC was utilized for the examination of relative displacements and strain gradients within the presented practical experiments. A gom ARAMIS 12M adjustable base system was introduced under use of the following configurations and parameter settings. The ARAMIS 12M system comprises two cameras with 12 megapixels resolution (4096 × 3000 pixels) which are coupled to two blue LED lights (24 VDC, 16 W, 10° projection angle, IP64 protection), all which are equipped with polarized filters for better specimen illumination without outer illuminating disturbances. The rate of image capturing was set to 2Hz and synchronously the channels of the universal testing machine, i.e., force and displacement were recorded. From the calibration volume which measured 200 × 145 × 130 mm^3 (length × width × depth) and the local resolution of 23.7 pixel/

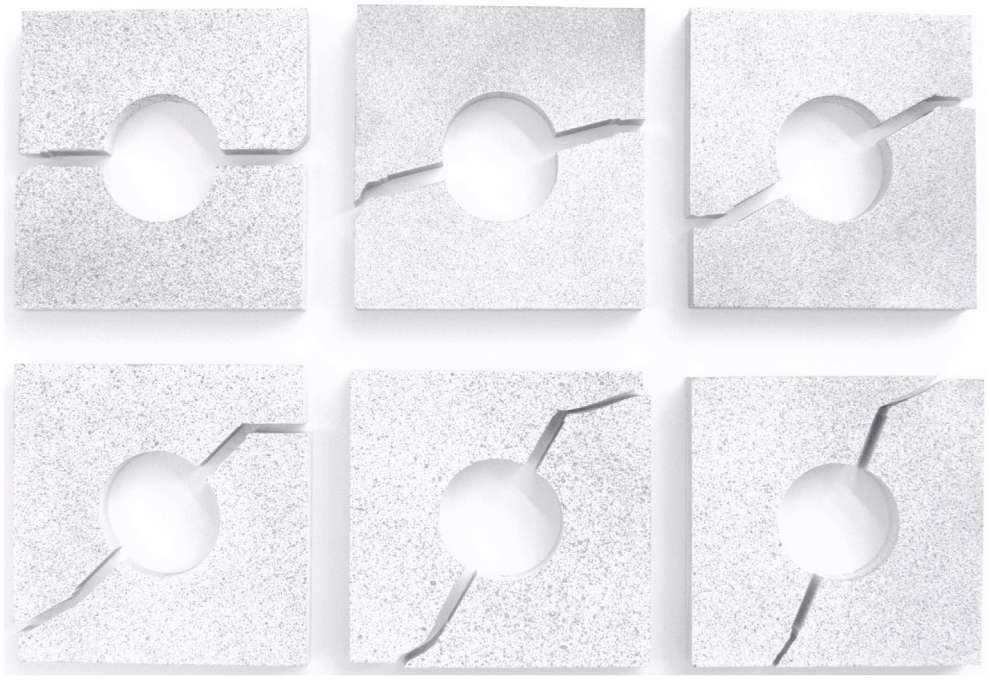

Fig. 10 – Fractured specimens with different crack orientation angles and crack propagation directions.

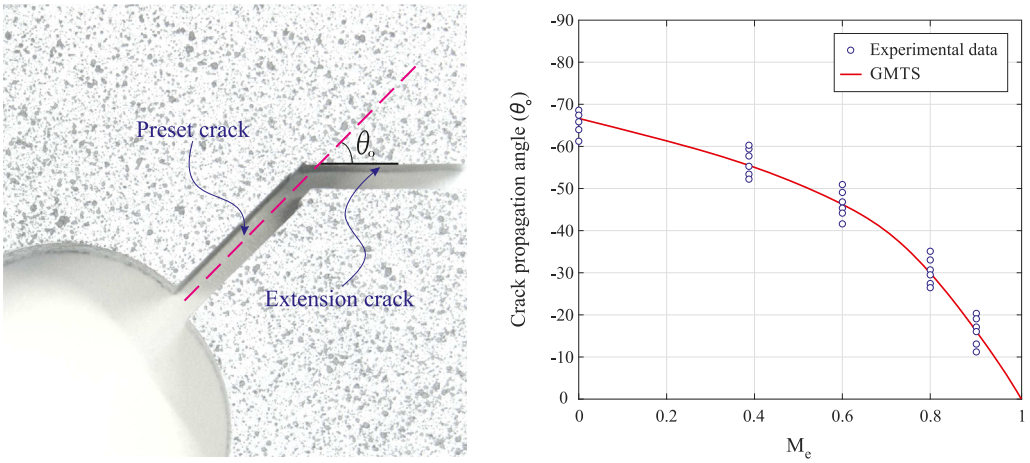

Fig. 11 – Crack propagation angle (θ_o) in a fractured specimen (left), and comparison of θ_o by GSED criterion and experimental tests (right).

mm, a facet size of 14 pixels and a point distance of 14 pixels resulted from the stochastic spray paint pattern. In average, the HCSP specimens provided a total number of evaluation points of about 11,000 points. In the gom ARAMIS software of the same name, local displacements and strains are calculated from the stochastic spray pattern, which was applied on the specimen surfaces. For this work, the calculation of strain followed the program standard algorithms summarized in the ZEISS Quality Tech Guide [39].

During the experimental procedure as already mentioned, the specimens were captured by DIC. In detail, a trigger signal was used for both machines (testing machine and DIC) as soon as a tensile force of 20 N was achieved. After specimen fracture, the synchronized DIC record was stopped manually. From the experiments, i.e., tensile tests and test of HCSP specimens, local displacements were evaluated to exclude any influence of the machine stiffness and utilized assemblies. Strain was evaluated by a virtual extensometer from the tensile tests. From the hole fracture tests, the strain gradients near crack initiation were of central interest, next to the force displacement curves. In addition to the strain maps captured from the spray painted surfaces of the HCSP test coupons, strain was averaged in a narrow circle of 2 mm radius around the crack tip to examine critical strain as a function of displacement.

Fig. 12 shows the test setup with a superposition of the DIC captured strain map, and the curves obtained when plotting critical equivalent v. Mises strain at the crack tip over experimental displacement for a representative specimen for each crack initiation angle on HCSP specimens.

As seen from the plots in Fig. 12 right, critical strain agrees with the load–displacement plots of Fig. 8. The highest load and strain values are obtained from the specimen with 68° of crack initiation angle β (pure mode II fracture condition). With decreasing crack initiation angle, load and strain decrease during mixed mode fractures until reaching similar values for initiation angles between 30 and zero degrees (the latter representing pure mode I fracture). In this range ($\beta = 0° \ldots 30°$),

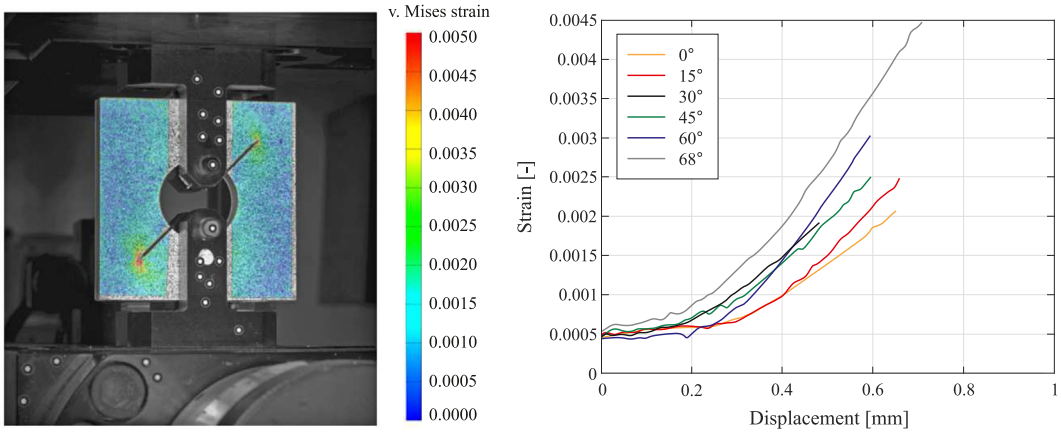

Fig. 12 – An example of von Mises strain map obtained from the surface of a 45° HCSP specimen at the critical time frame directly before brittle fracture (left), and evaluation of critical fracture strain in a close area around the crack tip over experimental travel and as a function of crack initiation angle (right).

slightly higher displacements are observed with decreasing initiation angle.

Strain maps are captured by DIC throughout the experimental procedure on tensile testing HCSP specimens. Fig. 12 left, shows an example of strain map captured just before fracture for a specimen with 45° crack initiation angle. V. Mises equivalent strain is scaled in between zero and 0.0050. In deed, a similar equivalent strain plot is observed compared to the qualitative stress maps obtained from FEM and shown in Fig. 1. Hence, by qualitative means, the DIC method validates the simulation model, which can be applied for further studies on tensile testing HCSP specimens. Fracture strain ε_f values of 3.0 percent engineering strain were evaluated from uniaxial tensile tests. Compared to the illustrated example of a strain map for 45° in Fig. 12 left and the plots of critical fracture strain over displacement in Fig. 12 right, significantly lower strain values in between 0.002 and 0.0045 are obtained from the crack tips of the HCSP specimens due to provoking mixed-mode fracture at a sharp pre-cracked edge.

5. Conclusion

As 3D-printed parts have promising potential for applications as structural or functional elements in different engineering fields, their mechanical strength has gained considerable importance. In the current study, we used the SLA 3D printing process to fabricate holed and pre-cracked square plate specimens. A full range of mode mixities in fracture can be achieved by changing the crack orientation angle. In this study, the crack orientation angle was changed from 0° to 60° with intervals of 15°. The finite element analysis was utilized and various mode mixities were observed (pure mode I to pure mode II). The numerical simulations show that the mode I geometry factor was decreased with an increase in crack orientation angle, but there was an opposite tendency in the mode II geometry factor. A series of fracture tests was performed on SLA 3D-printed specimens and stress intensity factors (K_I and K_{II}) for different specimens are obtained. Experimental tests show that the fracture load increases as the orientation angle increases. In addition, it was observed that only in pure mode I ($\beta = 0°$), the crack propagated in the same direction as the original crack. The crack propagation angles for different mode mixities are determined and presented. The results of the conducted simulations are comparable with those from the experimental side, qualitatively and quantitatively. The generalized strain energy density was used and a good agreement between experimental results and theoretical prediction is obtained. The presented results are beneficial for optimization, further numerical analysis, and next designs of SLA 3D-printed structural elements fabricated by the SLA printing process.

Declaration of Competing Interest

The authors declare that they have no known competing financial interests or personal relationships that could have appeared to influence the work reported in this paper.

REFERENCES

[1] Gibson I, Rosen D, Stucker B, Khorasani M. Additive manufacturing technologies. Springer; 2021.
[2] Mantihal S, Kobun R, Lee BB. 3D food printingof as the new way of preparing food: a review. Int J Gastron Food Sci 2020;22:100260.
[3] Mohammed AA, Algahtani MS, Ahmad MZ, Kotta S. 3D printing in medicine: technology overview and drug delivery applications, Ann. 3D Print. Med 2021;4:100037.
[4] Reddy KVP, Mirzana IM, Reddy AK. Application of additive manufacturing technology to an aerospace component for better trade-off's. Mater Today Proc 2018;5:3895–902.
[5] Nasiri S, Khosravani MR. Progress and challenges in fabrication of wearable sensors for health monitoring. Sens Actuators, A 2020;312:112105.
[6] Branco R, Costa JD, Ferreira JAM, Capela C, Antunes FV, Macek W. Multiaxial fatigue behaviour of maraging steel produced by selective laser melting. Mater Des 2021;201:109469.
[7] Joshi SC, Sheikh AA. 3D printing in aerospace and its long-term sustainability. Virtual Phys Prototyp 2015;10:175–85.
[8] Khosravani MR, Haghighi A. Large-scale automated additive construction: overview, robotic solutions, sustainability, and future prospect. Sustainability 2022;14:9782.
[9] ISO/ASTM 52900. Additive manufacturing - general principles - terminologys, standard. ISO/ASTM; 2015.
[10] Zhang F, Zhu L, Li Z, Wang S, Shi J, Tang W, et al. The recent development of vat photopolymerization: a review. Addit Manuf 2021;22:102423.
[11] Davoudinejad A. Handbooks in advanced manufacturing additive manufacturing. Elsevier; 2021. p. 159–81. Ch. Vat photopolymerization methods in additive manufacturing.
[12] Su F, Sabet FA, Tang K, Garner S, Pang S, Tolley MT, et al. Scale and size effects on the mechanical properties of bioinspired 3D printed two-phase composites. J Mater Res Technol 2020;9:14944–60.
[13] Khosravani MR, Zolfagharian A, Jennings M, Reinicke T. Structural performance of 3D-printed composites under various loads and environmental conditions. Polym Test 2020;91:106770.
[14] Daynes S, Lifton J, Lu WF, Wei J, Feih S. Fracture toughness characteristics of additively manufactured Ti–6Al–4V lattices. Eur J Mech Solid 2021;86:104170.
[15] Ameri B, Taheri-Behrooz F, Aliha MRM. Mixed-mode tensile/shear fracture of the additively manufactured components under dynamic and static loads. Eng Fract Mech 2021;260:108185.
[16] Frohn-Sörensen P, Geueke M, Engel B, Löffler B, Bickendorf P, Asimi A, et al. Fracture tailoring in 3D printed continuous fibre composite materials using the Phase field approach for fracture. Polymers 2022;14:1694.
[17] Bendine K, Gibhardt D, Fiedler B, Backs A. Experimental characterization and mechanical behavior of 3D printed CFRP. Eur J Mech Solid 2022;94:104587.
[18] Wang K, Cai R, Zhnag Z, Liu J, Ahzi S, Peng Y, et al. Compressive behaviors of 3D printed polypropylene-based composites at low and high strain rates. Polym Test 2021;103:107321.
[19] Atakok G, Kam M, Koc HB. Tensile, three-point bending and impact strength of 3D printed parts using PLA and recycled PLA filaments: a statistical investigation. J Mater Res Technol 2022;18:1542–54.
[20] Doshi M, Mahale A, Singh SK, Deshmukh S. Printing parameters and materials affecting mechanical properties of FDM-3D printed Parts: perspective and prospects. Mater Today: Proc 2021;50:2269–75.

[21] Khosravani MR, Berto F, Ayatollahi MR, Reinicke T. Characterization of 3D-printed PLA parts with different raster orientations and printing speeds. Sci Rep 2022;12:1016.
[22] Hukpati K, Eliasu A, Tetteh F, Czekanski A, Boakye-Yiadom S. Effect of printing parameters on the structure and high strain rate deformation behavior of additively manufactured 316L stainless steel. Mater Sci Eng, A 2022;853:143710.
[23] Fu X, Zou B, Xing H, Li L, Li Y, Wang X. Effect of printing strategies on forming accuracy and mechanical properties of ZrO2 parts fabricated by SLA technology. Ceram Int 2019;45:17630–7.
[24] Quintana R, Choi JW, Puebla K, Wicker R. Effects of build orientation on tensile strength for stereolithography-manufactured ASTM D-638 type I specimens. Int J Adv Manuf Technol 2010;46:201–15.
[25] Hague R, Mansour S, Saleh N, Harris R. Materials analysis of stereolithography resins for use in rapid manufacturing. J Mater Sci 2004;39:2475. 2464.
[26] Stógerer J, Baumgartner S, Rath T, Stampfl J. Analysis of the mechanical anisotropy of stereolithographic 3D printed polymer composites. Eur. J. Mater. 2022;2:12–32.
[27] Li Y, Pavier MJ, Coules H. A new specimen for mixed mode I/II fracture of brittle and quasi brittle materials. Procedia Struct Integr 2020;28:1140–7.
[28] TR300 Resin, https://phrozen3d.com/products, accessed: 20.September.2022.
[29] ASTM-D638. Standard test method for tensile properties of plastics. ASTM International; 2003.
[30] Akbardoost J, Ghadirian HR, Sangsefidi M. Calculation of the crack tip parameters in the holed-cracked flattened Brazilian disk (HCFBD) specimens under wide range of mixed-mode I/II loading. Fatig Fract Eng Mater Struct 2017;40:1416–27.
[31] Hadei MR, Kemeny J, Ghazvinian A, Rezaeipoor A, Sarfarazi V. New development to measure mode I fracture toughness in rock. Period Polytech Civ Eng 2017;61:51–5.
[32] Karimi HR, Khedri E, Aliha MRM, Mousavi A. A comprehensive study on ring shape specimens under compressive and tensile loadings for covering the full range of I+II fracture modes of gypsum material. Int J Rock Mech Min Sci 2022;160:105265.
[33] Mousavi SS, Aliha MRM, Imani DM. On the use of edge cracked short bend beam specimen for PMMA fracture toughness testing under mixed-mode I/II. Polym Test 2020;81:106199.
[34] Ayatollahi MR, Rashidi Moghaddam M, Berto F. A generalized strain energy density criterion for mixed mode fracture analysis in brittle and quasi-brittle materials. Theor Appl Fract Mech 2015;79:70–6.
[35] Williams ML. On the stress distribution at the base of a stationary crack. J Appl Mech 1957;24:109–14.
[36] Smith DJ, Ayatollahi MR, Pavier MJ. The role of T-stress in brittle fracture for linear elastic materials under mixed mode loading. Fatig Fract Eng Mater Struct 2001;24:137–50.
[37] Y. Luo, M. C. Leu, Z. Li, A microcrack model and its significance to hydraulic fracturing and fracture toughness testing, in: Proceedings of 21st US symposium rock mechanics, Missouri, USA, 1980, pp. 581–590.
[38] Brugo TM, Campione I, Minak G. Investigation by digital image correlation of mixed-mode I and II fracture behavior of polymeric IASCB specimens with additive manufactured crack-like notch. Materials 2021;14:1–15.
[39] Introduction to digital image correlation and strain computation, https://www.gom.com/en/topics/digital-image-correlation, accessed: February.12.2022.